FULL PAPER

HelixJet: An innovative plasma source for next-generation additive manufacturing (3D printing)

Jan Schäfer[1] | Antje Quade[1] | Kerry J. Abrams[2] | Florian Sigeneger[1] | Markus M. Becker[1] | Candice Majewski[3] | Cornelia Rodenburg[2]

[1]Division Materials and Surfaces, Leibniz Institute for Plasma Science and Technology, Greifswald, Germany

[2]Department of Materials Science and Engineering, University of Sheffield, Sheffield, UK

[3]Department of Mechanical Engineering, University of Sheffield, Sheffield, UK

Correspondence
Jan Schäfer, Leibniz Institute for Plasma Science and Technology, Felix-Hausdorff-Str. 2, 17489 Greifswald, Germany.
Email: jschaefer@inp-greifswald.de

Funding information
UK Research and Innovation, Grant/Award Numbers: EP/P006566/1, EP/N008065/1; Royal Society, Grant/Award Number: IE160969

Abstract

A novel plasma source (HelixJet) for use in additive manufacturing (AM)/3D printing is proposed. The HelixJet is a capacitively coupled radio frequency plasma with a double-helix electrode configuration that generates a surprisingly stable and homogeneous glow plasma at low flow rates of argon and its mixtures at atmospheric pressure. The HelixJet was tested on three polyamide powders usually used to produce parts by laser sintering, a powder-based AM process, to form local deposits. The chemical composition of such plasma-printed samples is compared with thermally produced and laser-sintered samples with respect to differences in morphology that result from the different thermal cycles on several length scales. Plasma prints exhibit unique features attributable to the nonequilibrium chemistry and to the high-speed heat exchange.

KEYWORDS

additive manufacturing, electron microscopy, plasma printing, polyamide, thermography
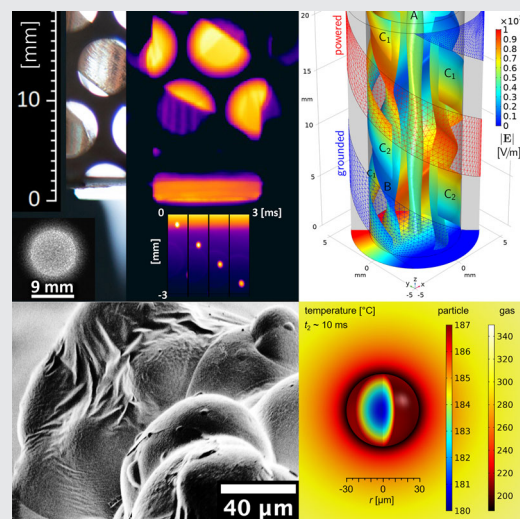
1 | INTRODUCTION

In additive manufacturing (AM) free form parts are fabricated by automatic deposition of multiple consecutive layers of material directly from a three-dimensional (3D) computer-aided design (CAD) file, thus removing the need for moulds or machining.[1] The 3D-printed structures can be obtained through different routes, classified according to the International Organization for Standardization (ISO)/American Society for Testing and Materials (ASTM) 52900:2015 as follows: binder jetting, directed energy deposition (DED), material extrusion (ME), material jetting (MJ), powder bed fusion (PBF), sheet lamination (SL), and Vat

photopolymerisation (VP). One of the most common PBF-based polymer-AM methods is laser sintering (LS). In LS, a layer of powder is spread over a build platform, following which selected regions of this layer are selectively melted by a laser over cross sections determined in the CAD file.[2]

By far the most exploited class of materials for 3D printing are polymers. This is not surprising given that polymers can be 3D printed by a number of different processes, with many AM techniques utilising thermoplastic or thermoset polymers as build materials. Plasma treatments are already integrated into many of these processes, for example, to improve adhesion between layers produced by ME or for better surface quality of PBF-fabricated parts. In addition, plasma treatment of powders before PBF leads to a reduction in porosity due to better wetting of solid surfaces by the melt.[3] Plasma spraying of polymers might also be considered as DED, as these systems have the ability to process large build volumes, at relatively high deposition rates and uses an articulated energy source with a strong energy coupling to the feedstock. The feedstock can be deposited directly onto existing components and has the potential to change chemical composition within a build to produce functionally graded materials (see ASTM F3187-16). However, in ASTM F3187-16, simple coating deposition systems are not considered to be DED for 3D printing because the latter must also have the ability to build layer-by-layer according to the CAD file.

It was shown decades ago that polyamide 11 (PA 11) can be plasma-sprayed into coatings using a plasma arc source, where the PA powder is fed into the flame of the plasma torch.[4] However, high arc powers (30 kW) were needed to melt the particles leading to a substantial weight loss of the feedstock due to thermal degradation. Both melting and degradation showed strong size effects resulting in major defects (e.g., unmelted particles, cracks, and pores). The best balance was found for PA 11 particles with sizes between 40 and 60 μm; but when compared with bulk material, the plasma-sprayed polyamide coatings exhibited a lower tensile strength and a brittle stress-strain characteristic—this brittle behaviour can also be observed in LS parts. Even for a given particle size, there are large temperature gradients within this arc plasma jet meaning that satisfactory coatings can only be produced for certain angles of feedstock injection. It follows that to obtain high quality coatings, a plasma source with a homogenous temperature distribution along its central axis is needed to ensure a high degree of melting.

This together with the requirement for layer-upon-layer deposition, places two further demands on the plasma source: (a) the ability to provide a well-defined lateral deposition spot (pixel) and (b) a temperature profile along the jet axis that allows the deposition of subsequent layers without causing thermal degradation. These conditions cannot be fulfilled by an arc plasma or similar sources, meaning innovative plasma sources are needed. The self-organisation phenomena observed in a nonthermal atmospheric pressure plasma jet have generated fresh ideas for homogenising the contracted discharge within the helical dynamics of filaments.[5] In a self-organised plasma jet, filaments are helically shaped and rotate with a velocity that depends on the inclination angle or helicity of filaments. Hence, the idea of double-helix electrodes is proposed for the new plasma jet, HelixJet. To provide a proof of principle, the treatment of polyamide 12 (PA 12) by HelixJet was chosen because PA 12 is widely used in the LS process.

PA 12 is the most common polymer in LS due to its mechanical properties and its favourable thermal characteristics for sintering. These characteristics (e.g., a relatively low melting temperature and a large window between the melting and crystallisation temperatures) render PA 12 as one of the most reproducible materials for use in LS. However, there are issues to overcome in terms of part properties and the overall efficiency of the process.[6] Though some parts produced by LS tend to perform similarly to more traditional techniques, such as injection moulding, in some cases (e.g., tensile strength), they perform poorly in others (e.g., elongation at break). In particular, the levels of porosity encountered within the parts tend to lead to a more brittle failure under tension, meaning, it is common to observe ductility that is an order of magnitude lower than for injection moulding.[7] It has been suggested that porosity is responsible for the large variability in LS parts,[8] and a number of attempts have been made to reduce this, including the plasma treatment of powders before sintering.[3,9–11] Although such plasma powder treatment processes could be scaled to the kilograms quantities needed per LS run, this concept has not been taken up widely;[12] presumably for two reasons: (a) The degree of surface functionalisation resulting from the treatment is markedly reduced within hours[12] and (b) the time and temperature need to be tightly controlled to avoid the degradation of the powders.[10,11] Even without plasma pretreatment, the powder degradation variations resulting from different time–temperature cycles are thought to be responsible for property variations in LS parts.[6] The LS process requires preheating of the base powder to a temperature slightly below the melting temperature to prevent "curl" of parts.[13] As a consequence, changes to the molecular weight and crystallinity of unsintered powder also occur.[14,15] At a certain point, the powder can no longer be processed, meaning this preheat stage adds time, cost, and complexity to the process.[14] The potential to process and deposit the powder directly where needed, rather than through selective sintering of a layer, would therefore provide a clear benefit.

2 | EXPERIMENTAL SECTION

2.1 | Powders and LS

Several grades of commercially available polyamide 12 (PA 12) were selected for this study: PA2201, PA2200, and PA2221, all from EOS GmbH. Samples produced from these powders are labelled in this study as 1, 2, and 3, respectively. The producer specifies mechanical and thermal properties, for example, strain at break: 15 % (PA1), 4–18 % (PA2), 4–16 % (PA3), vicat softening temperature: 163 °C (PA1 and PA2), melting temperature: 176 °C (PA1 and PA2) and 187 °C (PA3). The principal differences between these powders are in terms of processability and part properties. The common properties of PA 12 have been applied for simulation of particle heating: density of bulk material $1.01 \, g/cm^3$, thermal conductivity $0.51 \, W/(m \, K)$ and specific heat capacity $1.75 \, J/(gK)$.[16] Note that mass density varies depending on its form (powder or bulk). Thus, the specified density of powder is $0.93 \, g/cm^3$ (PA1 and PA2) and $0.97 \, g/cm^3$ (PA3).

Parts were produced on an EOS Formiga P100 LS system, using the default parameters for PA 12. They exhibit a range of morphologies with different degree of order at macroscopic and microscopic scales. Figure 1b shows the typical powder shapes and sizes on the surface of a LS object (sphere in Figure 1a). Figure 1c demonstrates the polycrystalline structures combining amorphous zones with lamellas of crystalline PA 12.

To compare the structure and chemistry of the plasma-manufactured samples, several samples were produced by LS (labelled with L), and melting of powders on a glass substrate for one hour at 190 °C (labelled with H). For the LS process, the following parameters were applied: Power 21.0 W, spacing 0.25 mm, scan speed 2500 mm/s, and beam offset 0.150 mm, leading to a manufacturing speed of $20 \, cm^3/hr$.

2.2 | Plasma source and processing of powders

The HelixJet is an atmospheric pressure capacitively coupled plasma source operated with radio frequency (RF) power applied to two double-helix electrodes. The electrodes are placed outside a quartz tube fed by the working gas, in this case argon. The specification of the HelixJet and operation conditions used in this study are listed in Table 1. The description of the design, corresponding electric field and thermal properties of the plasma source are presented in the results section.

Many concepts for continuous powder feeding that would be compatible with the HelixJet exist, for example, gravity-based systems for LS.[17] Continuous feeding in the context of plasma powder treatments was extensively reviewed recently.[12] Here, a single shot of powder (10 mg) was fed into the plasma by a dosing spoon in the upper part of the HelixJet. Thus, as the powder dose falls, the gas flow drives the particles through the plasma column. Because of the particle dimensions, the velocity of the gas determines the residence time of the particles in the plasma. In this case, the residence time is in the range of 50 ms (plasma column of 6 cm, 50 W, and 1 slm). The discharge was switched off immediately after deposition of the single dose to eliminate prolonged exposure by the plasma. The treatment speed of 200 mg/s was achieved by this setting. The samples prepared with the plasma process are labelled with P.

2.3 | Diagnostics and characterisation methods

Morphological investigations of deposits on the mm scale were carried out by light photography. The microscale and nanoscale morphology was investigated by scanning electron microscopy in secondary electron (SE) and back-scattered electron (BE) imaging modes. High-resolution top views were provided with a JSM 7500F (Jeol, Japan), which employs a field emission gun and two detectors used in this study: SE in-lens detector (maximum specified resolution of 1.0 nm) and low-angle BE detector with maximum resolution of at least 5 nm. The cross sections were observed in a Helios Nanolab G3 UC in a low-voltage ultrahigh resolution mode with no conductive coating.

Chemical analysis included a combination of Fourier-transform infrared (FTIR) spectroscopy and X-ray
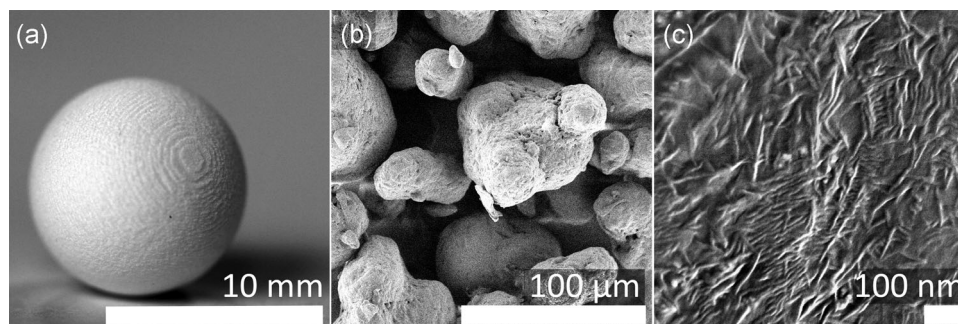
FIGURE 1 Laser-sintered polyamide sphere L1. Light photograph (a) details of surface morphology at low (b) and high magnification (c) obtained by scanning electron microscopy of secondary electrons

TABLE 1 Specification of the plasma source and deposition conditions applied in plasma printing of polyamide 12

Parameter	Quantity, ranges	Set values
Geometry of the tube (quartz)	0.7 cm (inner diameter), 12 cm (length)	–
Geometry of the electrodes (copper)	Nine turns, 57° inclination, 5 mm distance, width 5 mm (flat wire)	–
Electric power	30–100 W, 13.56 MHz, 27.12 MHz	50 W, 27.12 MHz
Gas flow	100–2000 sccm, Ar and its gas mixtures	1000 sccm Ar
Treated materials	Organic vapours, powders, small objects < 6 mm	PA 12 powders
Depositions	PECVD, Single powder shot (SPS), footprint area 1 cm^2	SPS 10 mg in 50 ms
Substrate	Dielectric or metallic below the tube (effluent)	Glass slides ($z = -2$ mm)

Abbreviation: PECVD, plasma enhanced chemical vapor deposition.

photoelectron spectroscopy (XPS). An FTIR spectrometer (Perkin Elmer) with a diamond-based attenuated total reflection (ATR) module allowed the analysis of samples in the mid-infrared range (700–4000 cm^{-1}). Elemental composition and bonding was analysed by XPS, via an Axis Ultra DLD (Kratos Analytical, UK) with Al K_α radiation (15 kV, 10 mA for survey spectra and elemental scans, and 15 kV, 15 mA for highly resolved measured C 1s and O 1s peaks). Three spots at different positions on each sample were analysed and averaged. Data acquisition and processing were carried out using CasaXPS (Casa Software Ltd.). After subtraction of the Shirley background the O 1s peaks were fitted using a Gaussian–Lorentzian GL (30) peak shape.

Two high-speed (HS) cameras were used for the characterisation of the HelixJet. The homogeneity of the discharge was investigated with VIS photography in the range of 200–900 nm at exposure times from 3 to 100 ns (660 × 660 pixels), by means of a PI-MAX4 (Princeton Instruments). The HS camera was oriented in the discharge tube to visualise the radial profile of plasma emission. An infrared HS camera SC6801 (FLIR) was employed for the investigation of surface temperature in the calibrated range from −10 °C to 350 °C. For thermography of the HelixJet, a 50-mm IR objective was utilised and in particular, the surface temperature of the quartz tube was investigated (565 fps, 640 × 512 pixels). For the temporally resolved measurements of particle processing in the plasma effluent, a 1:1 IR microscope objective (2,094 fps, 160 × 128 pixels) was applied achieving a spatial resolution of about 20 μm. This allowed the capture of the smallest droplets of polyamide particles (original average size of ~60 μm) with a time step of 0.5 ms.

3 | RESULTS AND DISCUSSION

### 3.1 | Homogeneity of the HelixJet and electrical field simulation

The double-helix electrodes (see Figure 2a) were constructed perpendicular to the inclined filaments (ortholines)

observed in the nonthermal atmospheric pressure plasma jet to accelerate the gliding of filaments in the new plasma source, HelixJet.[5] Although the helical structure of the electrodes induces a complicated 3D structure of the electric field, initial experiments demonstrated that a noncontracted, mostly homogeneous discharge is generated in the HelixJet, as shown in Figure 2c, e. To explain this apparent contradiction, a first study was devoted to the determination of the electric field $\mathbf{E}(\mathbf{r}) = -\nabla\phi$ and its homogeneity. For this purpose, the Poisson equation

$$\nabla \bullet \varepsilon_r \mathbf{E}(\mathbf{r}) = \frac{\rho(\mathbf{r})}{\varepsilon_0},$$

with the vacuum permittivity ε_0 was solved in the solution domain shown in Figure 2a. Within this first approach, the space charge density $\rho(\mathbf{r})$ was neglected and appropriate values $\varepsilon_r = 1$ and 4.3 were used for the relative permittivity ε_r in the plasma zone and in the capillary, respectively. The solution domain is restricted in the axial direction to one turn of the electrodes, which are wound onto the capillary with a helix angle of 33°. Note that the ortholines to the electrode helix have the helix angle 57°, which corresponds to the helicity of filaments described in the previous study. Period boundary conditions were applied to link the bottom and top sides of the solution domain, and the voltages $V = 0$ and $V = 1$ kV were set to the grounded (blue mesh in Figure 2a) and powered (red mesh in Figure 2a) electrodes, respectively. The condition $\mathbf{E} \cdot \mathbf{n} = 0$ was used at the surfaces between the electrodes, where $\mathbf{n}$ denotes the normal vector from the surfaces.

The results obtained are presented in Figure 2a and show the 3D structure of the electric field using the isosurfaces A, B, C_1, and C_2, which represent constant values of the magnitude of the electric field |$\mathbf{E}$| as listed in the caption. The colour of the surfaces represents the electric potential ϕ. Representative axial ($y = 0$) and radial ($z = 5.4$ mm) cuts of the electric field |$\mathbf{E}$| are shown in Figure 2b and Figure 2d, respectively. The dielectric and plasma regions are separated
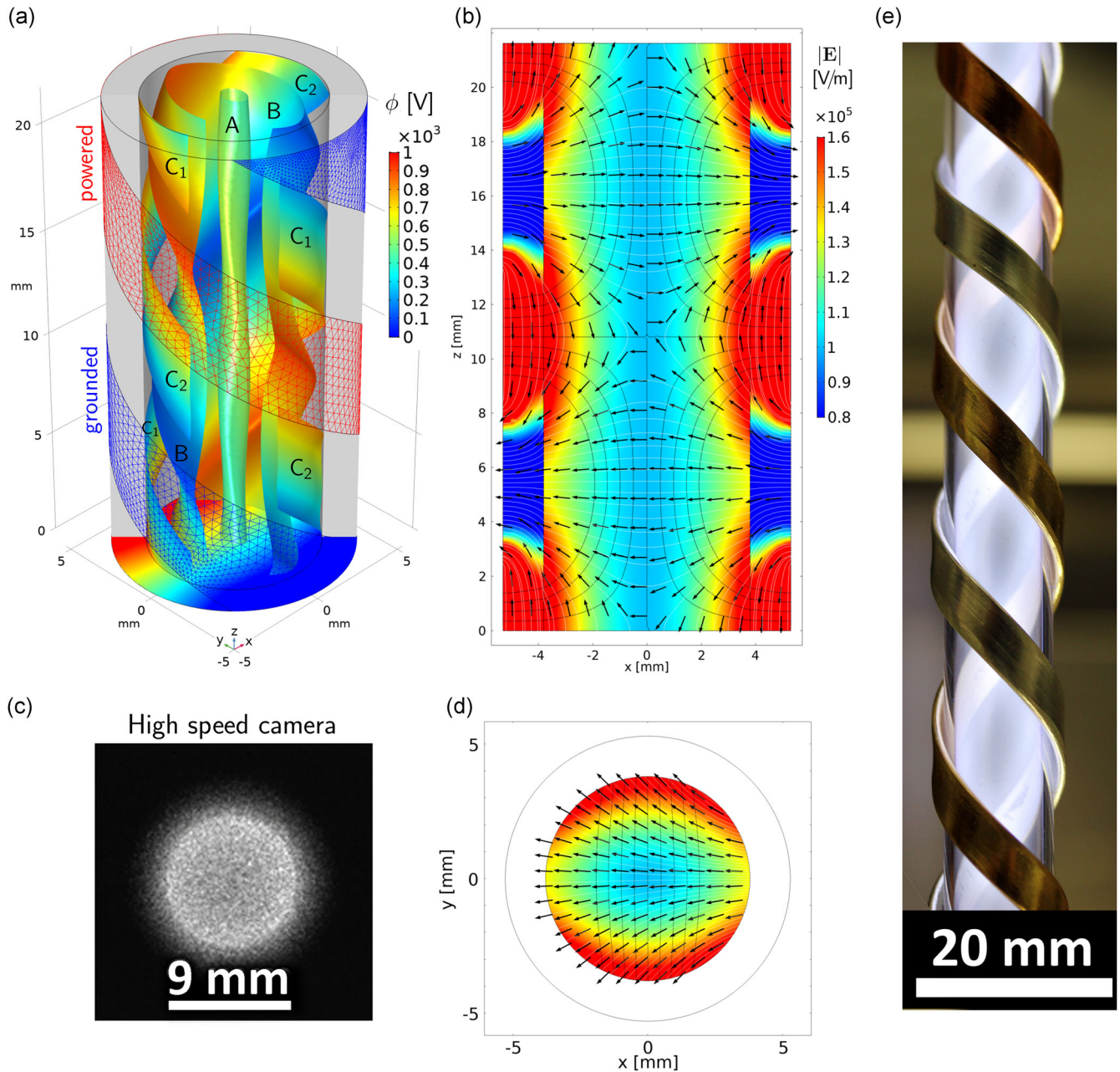
FIGURE 2 Predicted electric field in a section of the jet limited by one turn of both electrodes presented in a 3D plot (a) in a x–z cut at $y = 0$ (b) and in a x–y cut at $z = 5.4$ mm (d). The symbols in (a) denote isosurfaces with constant electric field magnitude |E| being equal to 102 kV/m (A), 130 kV/m (B) and 174 kV/m (C_1 and C_2). The experimental observations show an axial image taken by an HS camera PI-MAX4 with the exposure time of 3 ns (c) and a side photo at 1/80 s by Canon EOS 600D (e)

in Figure 2b by vertical lines at $|x| = 3.8$ mm. These results demonstrate that the modulations of the electric field within the inner zone are limited to <50 %. This weak variation of the electric field magnitude may be an indication of the establishment of a homogeneous plasma in the inner zone as observed experimentally.

The HS imaging experiments of the discharge confirm that no filaments were formed in the HelixJet, but a homogeneous glow discharge column was developed in the tube. Only the modulation of emission due to the

frequency of the RF power remains. The homogeneity of the plasma column was proven by HS imaging with several sequences. Figure 2c shows an image that was obtained by applying the smallest exposure time of 3 ns.

3.2 | Thermal characterisation of the HelixJet

Temperature control is the key to plasma deposition of polymeric materials with reproducible properties.[18]
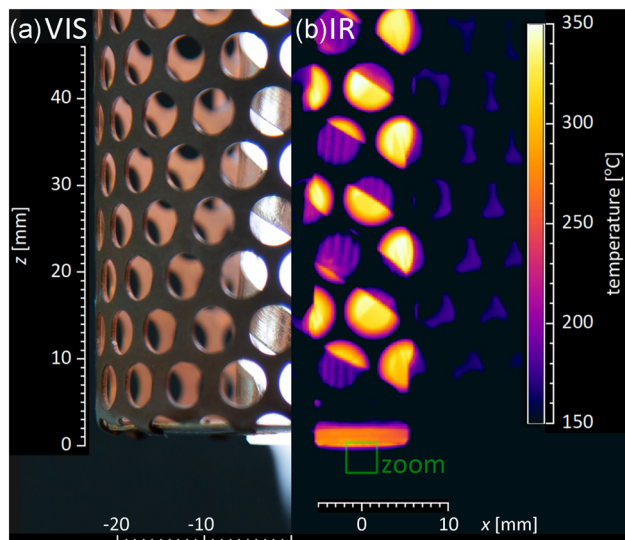
FIGURE 3 Photo (a) and IR thermal image of the HelixJet (b). The HS IR camera was focused at the area labelled "zoom" for IR measurement of the particle temperature (compare with Figure 4). HS IR, high-speed infrared

Figure 3 combines a thermographic image of the HelixJet with a VIS photo during stationary operation without powder particles in the plasma showing that the temperature of the capillary surface is about 350 °C. Thus, a neutral gas temperature, T_g, of approximately 427 °C can be expected in the active zone of the discharge, which is substantially higher than the melting temperature of 187 °C of PA 12. However, as particles are introduced and melted, PA 12 molecules evaporate and then quench the discharge. Thus, the T_g drops and the melting of particles is consequently stopped and the discharge can develop again. Therefore, we assume a dynamical equilibrium of the kinetic temperature near to the melting point of the polymer. This hypothesis was investigated by HS microscopic thermography of particles and corroborated by modelling.

The particle temperatures were measured as they leave the HelixJet by focusing a HS IR camera at the area labelled as "zoom" in Figure 3b. The results are shown in Figure 4. The temperature of the tube edge is approximately 200 °C and the particles leave the edge with surface temperatures between 160 °C and 190 °C (Figure 4c). The movement of one particle is demonstrated in Figure 4d by HS thermography at a frame rate of 2 kfps. The velocity of the particle is 0.63 m/s and its core temperature decreases with −12 °C/ms over a distance of 2 mm. Because of such a high cooling rate, it is likely that crystallisation occurs by homogeneous nucleation at the lower temperatures.[19]

The particle velocity and cooling rate are linked to the gas velocity. The latter depends on the applied gas flow rate Q at the inlet of the plasma jet and T_g can be controlled by the RF power coupled into the plasma. The measured particle velocity is in very good agreement with the results of a fluid dynamics model of the laminar gas flow in the tube of the HelixJet. The model shows that the gas velocity is largest at the centre of the plasma jet and decays parabolically towards the inner wall of the capillary. Maximum gas velocities in the range from 0.1 m/s ($Q = 0.1$ slm, $T_g = 300$ K) to 2.7 m/s ($Q = 1$ slm, $T_g = 1000$ K) are obtained by numerical solution of the stationary incompressible momentum Navier–Stokes equation using COMSOL Multiphysics®. Due to the low dimension of the particles, gravity effects are small compared with friction and the particles in the jet are driven purely by the gas flow. With this assumption, residence times in the range of 0.05 to 1.5 s can be estimated from the calculated gas velocities. To achieve a high throughput, this residence time should be minimised to such an extent that the required particle-melting temperature can still be achieved.

Therefore, to study the heating of particles in the argon gas stream, the time-dependent heat equation was solved numerically using COMSOL Multiphysics®. The simulation of the heating of particles with a diameter of 60 µm in the plasma with a predefined T_g predicts a thermalisation of the particles within 0.1 s. Hence, a fly path of particles in the active plasma of approximately 1 cm would be sufficient for future experiments.

Finally, the results of the IR imaging (see Figure 4c,d) suggest that the temperature of the particles does not rise substantially higher than the melting point confirming our initial hypothesis. The feedback mechanism between particles and plasma controls the evaporation of material and protects the particles against excessive thermal degradation, which is likely to play an important role in achieving deposits with reproducible properties.

The results from the heat-transfer model shown in Figure 4a,b demonstrate the change of the temperature distribution caused by ingesting a particle at the initial laboratory temperature into the hot gas ($T_g = 350$ °C). As can be seen in Figure 4a, the introduction of the particle leads to a quick drop of the gas temperature close to the particle. After approximately 0.7 ms, the particle core temperature reaches 35 °C while the particle surface has a temperature of about 46 °C at this instant (cf. Figure 4a). The melting point of 187 °C at the particle surface is reached after approximately 10 ms, at which point the temperature of the particle core is 180 °C (cf. Figure 4b).

The results above demonstrate how the process conditions can be adjusted and predicted from a combination of modelling, easily accessible parameters such as the flow rate and power coupled into the plasma
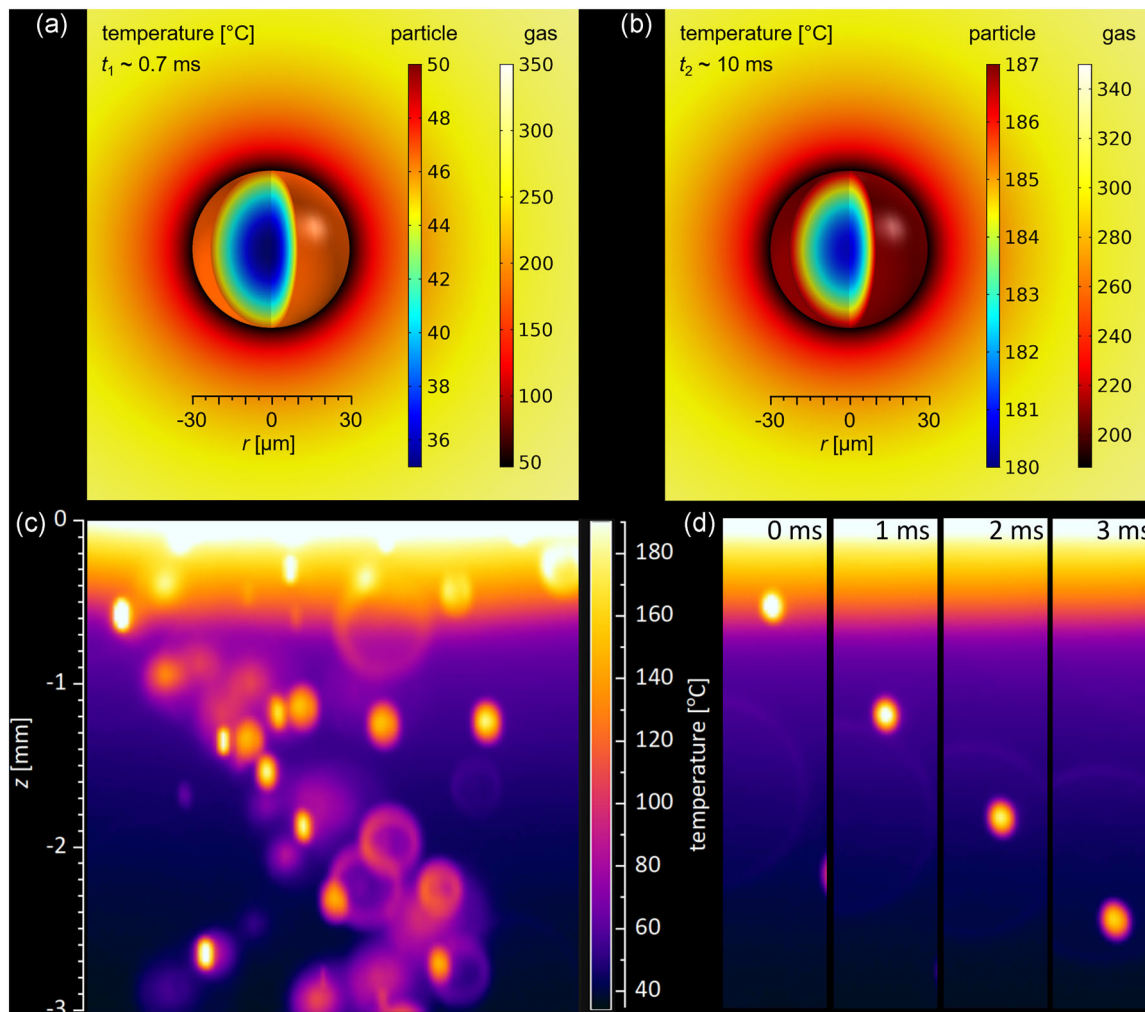
FIGURE 4 Temperature dynamics of particles. Particle and gas temperature obtained from heat-transfer simulations after $t_1 = 6.6 \times 10^{-4}$ s (a) and $t_2 = 9.3 \times 10^{-3}$ s (b), both for a background temperature of 350 °C; high-speed IR (infrared) thermography of particles in the effluent at 2 kfps: particle temperature from zoomed area indicated in Figure 3b (c), tracked single-particle movement (d). Note that in (c) and (d) different sizes of particles are caused by IR imaging optics being focused to the axis of the jet. Particles out of focus appear with different size and with incorrect temperatures

enabling a model-based optimisation of the process for different particle sizes and powder types.

3.3 | Morphological characterisation of plasma-manufactured samples

The typical sample, P1, was deposited by HelixJet and is shown in Figure 5a (compare to L1, Figure 1a). The plasma deposit is confined to an area that closely corresponds to the diameter of the quartz tube (7 mm) and has a typical Gaussian profile with the width $2\sigma = 7.97 \pm 0.05$ mm and the maximum at the axis of the jet corresponding to the gas flow profile (Figure 5c). The process excels with a maximum deposition rate of 2–3 µm/ms (200 mg/s). Some micron-scale roughness related to the powder size is visible here, which hints that particles approaching the surface are either partially

melted or the melted droplets are cooled quickly before landing, which is consistent with the results of section 3.2. The cross-section of the sample (Figure 5b) visualised by secondary electron imaging (SEI) evidence two important features. Although the original form of particles or droplets is partially conserved, they are melted together. Moreover, the morphology indicates a sufficient cohesion of the produced sample suggested by lamellas, which are spread over several microns in the vertical fracture surface (Figure 5b) in dark orange.

The comparison of microscale and nanoscale morphology between L, P, and H samples is demonstrated by SEM analysis (Figure 6). The purely thermally treated powder surface (H samples) exhibit less surface roughness as the original form of the particles disappeared completely over the field of view with a width of 1.2 mm (Figure 6a,c,e), which represent the surface topography.
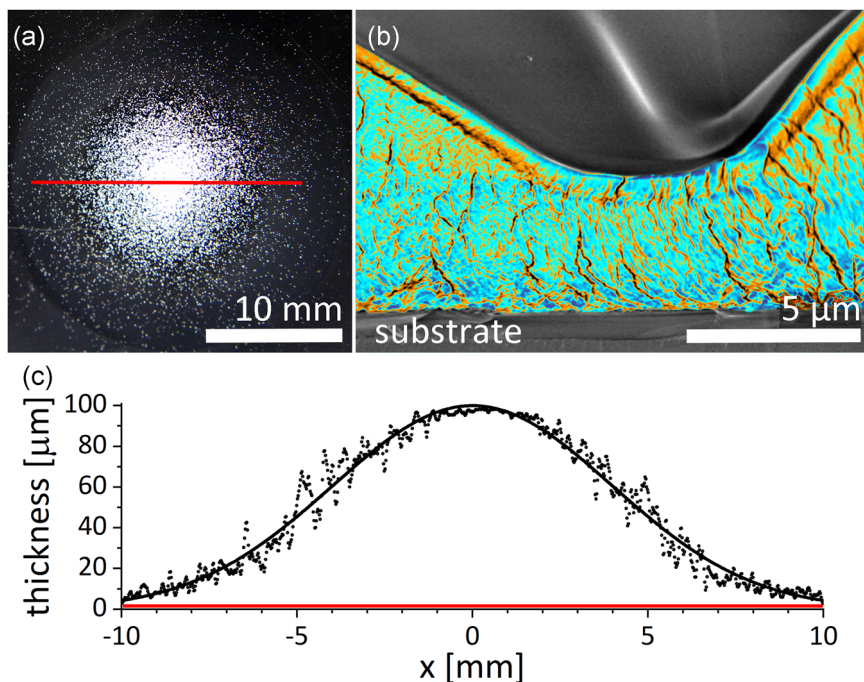
FIGURE 5 Top view photo (a) taken from particle deposition (sample PA1) on a black smooth plastic substrate; secondary electron imaging (SEI) of the local deposit cross-section (b); and thickness profile of the deposit (c) along the red line marked in (a). The saddle-shaped cross-section (b) results from the original shape of two adjacent melted particles. The false-colour scale of SEI was applied to enhance fine gray scale variations: blue, low SEI emission (dark); orange, high SEI emission (bright)

These images were collected with a secondary electron (SE) detector at a low primary beam accelerating voltage of 1 kV. Figure 6a reveals that in the LS sample all powder particles are still visible, whereas the plasma-printed area (cf. Figure 6c) contains only a few clearly identifiable powder particles that are embedded in large smooth areas. Thus, on this length scale, the plasma-printed material combines features that are characteristic of LS and thermal annealing, respectively.

This shows promising results for the establishment of 3D plasma printing. First, the partially melted particles can serve as coalescence centres and thus ensure confinement of the deposited materials to the plasma jet exposed area. Second, a smoother compact composite is likely to achieve higher mechanical properties as it is known in LS that the mechanical properties of parts improve when the proportion of non-melted particles is reduced.[20] Indeed, the connection between particles is made via partially melted material.[21] However, global shrinkage possesses a challenge in LS.[22] The coherent connection in plasma printing has been demonstrated in Figures 5b and 6c. Moreover, local connections (see inset in Figure 6c) by folded structures between particles indicate an efficient mechanical relaxation, which might prevent the substantial shrinkage of final parts by plasma printing.

The mechanical properties are determined by the molecular arrangement of PA 12 on microscopic scales, which is affected by the degree of melting.[19] Therefore, BEI was used to reveal any small density differences in the polymers as a result of local crystallinity variations.[23] Due to their higher density, crystalline areas appear brighter than amorphous areas.[23] Figure 6b,d,f show BE images

covering $4 \times 3\,\mu m^2$ from each sample. Due to the design of BE detectors, BEI requires a higher acceleration voltage of the incident electron beam (15 kV). As a result, Figure 6b,d,f contain some information that may have originated from several microns below the surface. In these BEI, false colouring was applied so that the bright (poly)-crystalline areas appear in orange tones while dark amorphous areas are in cyan tones. The coloured micrographs reveal that the spatial extent of ordered and disordered areas varies markedly depending on the deposition method. The H samples exhibit the highest degree of crystallinity (numerous appearances of spherulites), whereas L samples exhibit the smallest degree. Moreover, in all BEI, the presence of nanoparticles, which are assumed as nucleation centres of polymerisation, have been observed (dark dots). Their content, as well as the structure features in PA 12, are closely linked to chemical properties, in particular to the degree of crosslinking and polymerisation. Hence, the chemical analysis of samples is fully discussed in the next section.

3.4 | Chemical characterisation of samples

The chemical surface composition was determined by XPS. The atom percentages of the elements carbon, oxygen, nitrogen, and silicon are summarised in Table 2 for the powders (PA1, PA2, and PA3), LS sample (L1), plasma deposits (P1, P2, and P3), and deposits obtained by heating (H1, H2, and H3). Note that hydrogen cannot be determined by XPS. XPS revealed the overall similarity of all samples in terms of stoichiometry to PA 12. In
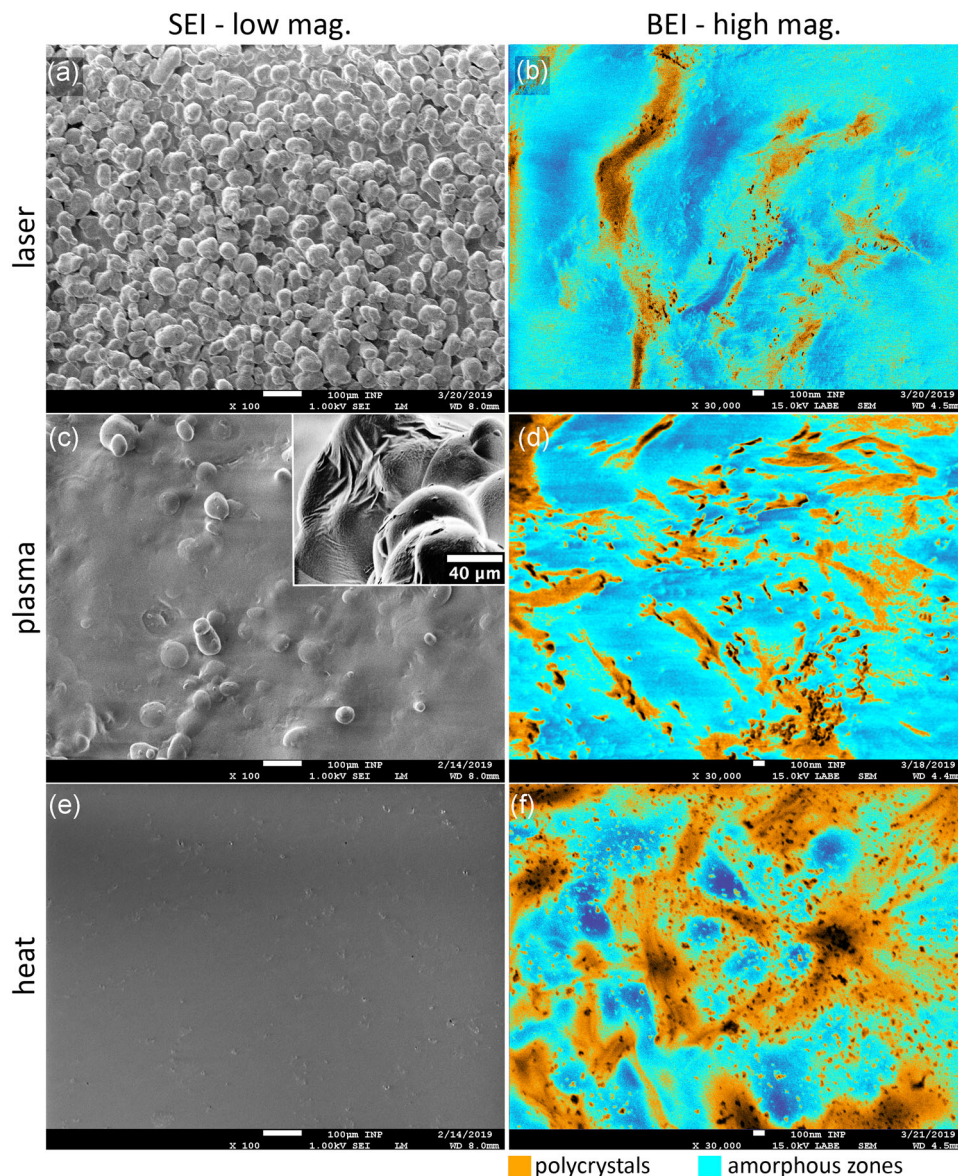
FIGURE 6 Scanning electron micrographs of a laser-sintered sample L (a,b), plasma-printed sample P (c,d), and sample prepared by the heat treatment H (e,f). All samples are imaged at low magnification with a secondary electron detector, SEI (a,c,e), and at high magnification with a backscattered electron detector, BEI (b,d,f). False-colour BE imaging was applied to better visualise the polycrystal (BEI bright orange) and amorphous (BEI dark cyan) zones

particular, nitrogen concentration approaches the ideal content of 6–7 atomic %, and small quantities of additives were observed: silicon (0–3 at.%) and phosphorus (below 1 at.%), as would be expected in powders designed for LS. In terms of oxygen content only, the heat-processed materials coincide with the content theoretically expected from the molecular structure of PA 12 while powders before processing exhibit an excess of oxygen. The plasma deposits contain less oxygen than the powders but more than the heat-processed samples. These observations could be explained by postpolymerisation as polyamide

TABLE 2 Element analysis of samples obtained by means of XPS (without hydrogen)

No.	C (at.%)	O (at.%)	N (at.%)	Si (at.%)
PA1, PA2, PA3	79–81	11–12	6–7	3
L1, P1, P2, P3	83–86	8–9	6	<2
H1, H2, H3	87–88	6–7	6	<1
PA 12 (ideal)	86	7	7	0

Abbreviations: H, samples preapared by heating of powder; L, laser-sintered samples; PA, polyamide; P, plasma deposits; XPS, X-ray photoelectron spectroscopy.

molecules are terminated with hydroxyl groups (R-OH), which polycondense and produce water.[14,24]

To test this hypothesis, the binding components of oxygen in the XPS O 1s spectrum were further investigated (see Figure 7 and Table 3). The processing of powders consistently reduced the hydroxyl groups in all samples to 8–30 % (related to carbonyl groups) compared with the raw powders with 44–50 % (C–OH/C=O), with shifts of Amide I and intensity of Amide A in FTIR spectra (Figure 8). This implies postpolymerisation and crosslinking of polymer chains in deposits, consistent with the predominance of polycondensation in PA 12.[15] Evidently, these reactions take place during all applied deposition methods. In particular, LS samples (L1) and samples prepared by plasma processing (P1–3) exhibit a similar degree of postpolymer-isation resulting in the oxygen concentration of 8–9 at.%, whereas the thermally processes material contains the expected 7 at.%. Note that the effect occurs on different time scales of 50 ms and 1 hr during plasma treatment and thermal processing, respectively. Hence, plasma processing accelerates the molecular kinetics dramatically. LS would be expected to produce a sample with a comparable mass to P1 (10 mg) in approximately 1 s. In parallel to the polymerisa-tion kinetics, the polycrystalline structure of the samples is also affected during processing.

A main structural feature in polyamides is the organisa-tion of the chains into well-defined two-dimensional (2D) hydrogen-bonded sheets, which are held together in 3D by van der Waals' interactions with similarities to β-sheets arrangements in silks.[26] The sheet alignment (antiparallel or parallel) is linked to that form in which the PA 12 crystallites. Crystallisation in the α-form (antiparallel) and γ-forms (parallel) is possible,[27] with the γ-forms being preferred.[28] The structural arrangement in the powders and as result of the different deposition methods can be probed by IR spectroscopy. In particular, the Amide I, II, and A as shown in Figure 8 are significant for qualitative interpretation of these structure changes, which correlate with XPS results.

The Amide I (Figure 8a) reflects the backbone con-formation and the hydrogen bonding pattern. The mode consists primarily of stretching vibration of C=O (76%) with small contribution of CN and CCN deformation. The position varies from 1635 cm^{-1} for the α-form and 1640 cm^{-1} for γ-form.[28] In Table 3, the position of Amide I is compared with the binding composition obtained with XPS. From both Table 3 and Figure 8, it can be seen that all thermally prepared samples have the peak at the smallest wavenumber of 1633 cm^{-1}, which is consistent with the α-form and that they have the smallest concentration of C–OH groups, whereas plasma prepared samples show peak broadening towards the higher wavenumbers (peaks at 1634 and 1636 cm^{-1}). Thus, the latter are likely to comprise of a combination of α and γ forms.
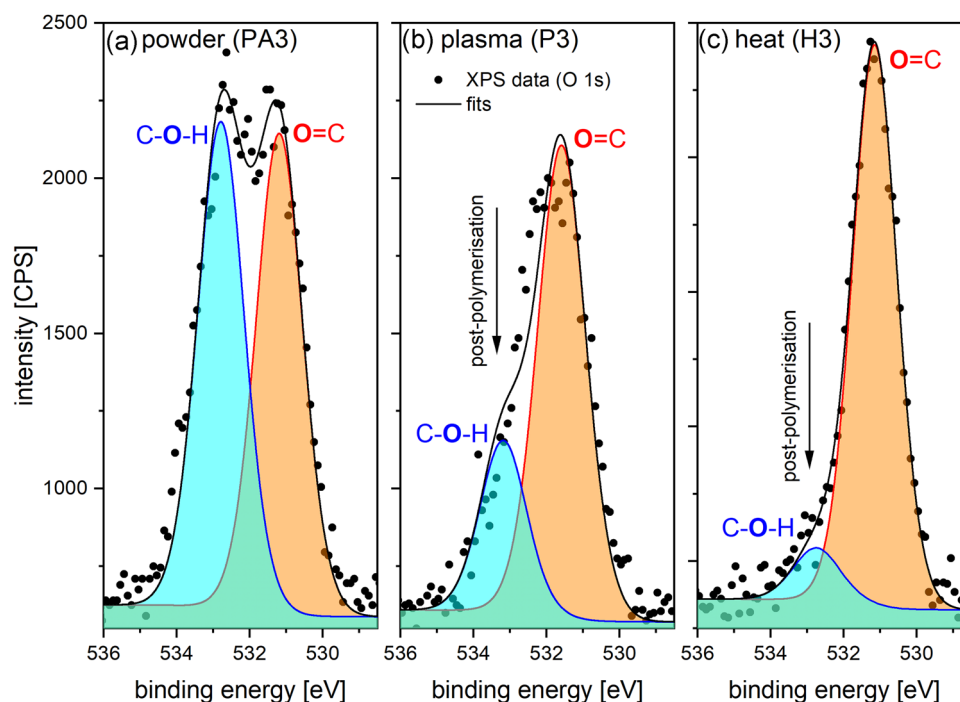

FIGURE 7 XPS analysis of O 1s peak of three classes of PA 12 samples: (a) PA3 powder, (b) samples produced by plasma processing, and (c) samples prepared by heat processing. For all materials, the two components of the peak were deconvoluted and the corresponding composition with respect to C–O–H (532.9 ± 0.2 eV) and O=C (531.3 ± 0.2 eV) bonding was quantified (see Table 3). PA, polyamide; XPS, X-ray photoelectron spectroscopy

TABLE 3 Red shift of Amide I in ATR spectra (Figure 8a) compared with reduction of hydroxyl groups (OH) in XPS spectra (Figure 7) of different polyamide samples investigated in this study

Samples	Amide I (cm^{-1})	[C–OH]/[C=O] (%)	Sample characterisation
PA1, PA2, PA3	1638–1637	44–50	Raw powders PA 12, γ-form dominates
L1, P1	1637	30–25	α- and γ-forms, slightly lower polycrystallinity, postpolymerised
P2, P3	1636–1634	26–24	α- and γ-forms, slightly higher polycrystallinity, postpolymerised
H1, H2, H3	1633	10–8	α-form dominates, intensive BEI, and spherulites (SEM)

Abbreviations: ATR, attenuated total reflection; BEI, backscattered electron imaging; PA, polyamide; SEM, scanning electron microscopy.
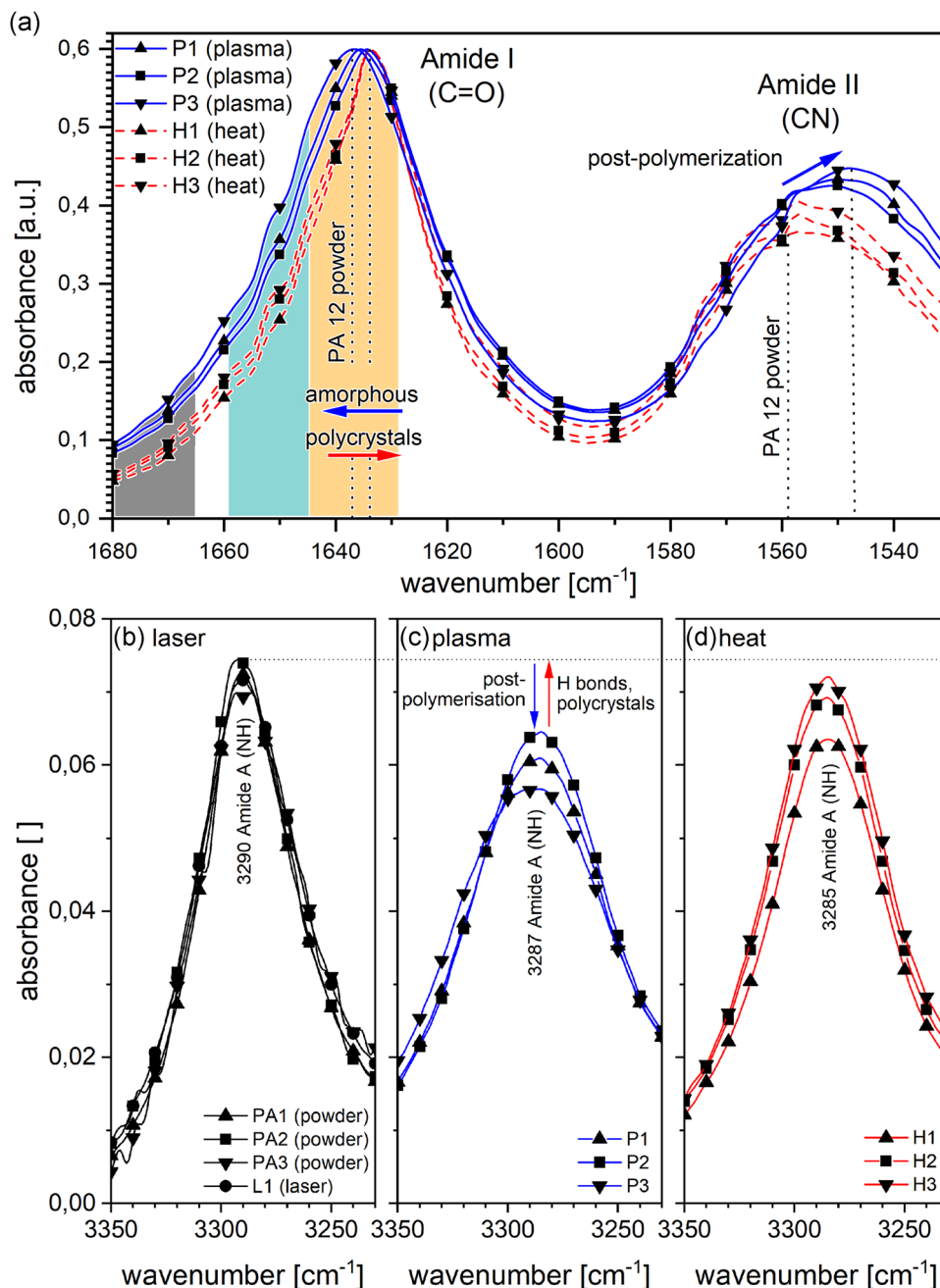
FIGURE 8 FTIR spectra of PA samples. Selection of significant peaks Amide I, II (a) and Amide A (b–d) indicate postpolymerisation and recrystallisation in plasma deposits (a,c), LS samples (b), and thermally prepared samples (a,d). The intervals of wavenumber in orange, cyan, and grey (a) mark regions of the ordered, disordered, and free hydrogen bonding conformation, respectively.[25] FTIR, Fourier-transform infrared; LS, laser sintering; PA, polyamide

The Amide II is related to the out-of-phase combination of bending NH (43%), stretching of CN (29%) with small contributions of bending C═O and stretching C–C and N–C, and is found at 1540 cm^{-1} for the α-form and 1563 cm^{-1} for γ-form, respectively.[28] However, the position and intensity of Amide II is also influenced by the change in CN bonds due to the postpolymerisation of the material. Thus, the shift of Amide II indicates the significance of postpolymerisation induced by the plasma treatment, while the shift of Amide I suggests an importance of recrystallisation induced by the thermal treatment. Both of these effects are consistent with results of XPS and BEI observation in the SEM. Moreover, for the plasma deposits, the shifts combined with peak broadening of the Amide I and II have been observed. This can be explained by the additional presence of the α-form in the material. Thus, both Amide I and Amide II bands point to the simultaneous presence of α- and γ-forms in plasma deposits. Note that the original powder (specifically PA1) is found to contain the α-form as determined by wide-angle X-ray scattering.[25] Note that the α-form can be obtained by controlled cooling of the melt.[25] As Section 3.2 demonstrates, the fast cooling experienced by the powder as it leaves that the HelixJet might explain the presence of the α-form, which is not usually formed under atmospheric pressure. As the cooling rate varies across the particle diameter, one might speculate that the layered structure in the plasma deposits (see Figure 5b) represents α- and γ-forms. The surface itself is covered by amorphous material, which also surrounds individual particles binding them together as can be seen in Figure 6c inset. The structure composition of the samples can be understood based on investigations for PA 11.[29]

It was reported that a peak position in the region marked in orange (Figure 8a) indicates the hydrogen bonding in an ordered conformation, while the cyan region is the disordered hydrogen-bonded Amide I.[29] Amide groups, "free" from hydrogen bonding, are found in the grey region when the distance between amide groups is so large and no hydrogen bonds are formed. It can be seen that the relative intensity in the disordered and "free" region is substantially larger in the plasma-deposited powders compared with thermal deposition. This is consistent with a reduction of amorphous material in the latter, which is present but within which spherulites can be detected (Figure 6f).

The Amide A band is sensitive to the strength of a hydrogen bond due to the stretching vibration of N–H and its peak position is a reflection of the average strength of hydrogen-bonded N–H groups.[29] In all samples, the position does not change significantly, but the absorbance of Amide A decreases slightly from the original material to the plasma deposits, where the band also appears much broader. The peak broadening is an indication of differences

in distances and geometries.[29] Thus, we can conclude that the broad peak observed in the plasma-printed materials is caused by a variety of distances and geometries, and thus may have the potential to reduce or avoid anisotropy of mechanical properties. The degree of disorder and mechanical properties should be controlled through the cooling rate and residence time in the HelixJet for which models are provided in Section 3.2.

4 | CONCLUSION

The novel HelixJet plasma source was used to deposit PA 12 powders at atmospheric pressure with deposition rates of 200 mg/s resulting in partially melted powders and strongly interconnected particles in the deposits. A confinement of the powder particle beam in the centre of the jet was achieved by the laminar gas flow, the discharge stability and by a radially and axially homogenous plasma. These conditions led to a Gaussian thickness profile of single-dose deposits on the mm-length-scale with a combination of chemical and morphological structures expected to benefit mechanical performance.

A first approach to a theoretical description of the HelixJet pinpointed the moderate alterations of the magnitude of the electric field as a reason for the unexpected homogeneity of the established plasma in the jet. The modelling of the heating of powder particles demonstrated that the particles reached the melting temperature at their surface while their core remain slightly colder. This can also be confirmed experimentally and explained with a self-regulation effect, where the exceeding of melting temperature and the increased evaporation would quench the plasma and drop the particle temperature below the melting temperature. This effect causes the presence of the combination of morphology features found in slow heat sintering and LS processes and can enable in perspective the plasma printing of 3D objects with comparable material properties as demonstrated here by SEM and chemical analysis.

The chemical analysis revealed that two fundamental processes should be considered in the 3D manufacturing from PA 12 by plasma treatment: (a) recrystallisation of PA 12 during heating and cooling and (b) plasma initiated postpolymerisation and activation of the polymer. During plasma printing, both these processes run synchronously on a time scale, which is much shorter than typically for LS or conventional thermal processing. Furthermore, the microscopic particle heating as well as the electric fields are described with models that can be coupled to the plasma parameters to obtain a unique morphology of plasma deposits. The latter results from the nonequilibrium chemistry in the nonthermal discharge and is reflected in

modifications of material polycrystallinity, crosslinking, and in the densification of the polymeric network.

On the basis of the feasibility experiments and modelling, an upscaling of the plasma manufacturing process using a HelixJet to speeds in the order of 1 cm³/min seems possible, although further work is needed to transform the HelixJet into a full-AM tool, for instance, introducing a continuous powder feed system and computerised control. However, the potential for constructing larger parts than possible in LS, in air and without the enormous quantities of waste powders, which drive up the cost, should provide the impetus to carry out such work. Moreover, the combination of HelixJet with laser beam manipulation might enhance the precision, speed, and controlled material structuring from microscopic to macroscopic level with a broad impact for many applications.

ACKNOWLEDGEMENTS

ORCID

Jan Schäfer http://orcid.org/0000-0002-0652-5057
Antje Quade http://orcid.org/0000-0003-0814-4319
Kerry J. Abrams http://orcid.org/0000-0002-2789-7204
Florian Sigeneger http://orcid.org/0000-0002-7238-6112
Markus M. Becker http://orcid.org/0000-0001-9324-3236
Candice Majewski http://orcid.org/0000-0003-3324-3511
Cornelia Rodenburg http://orcid.org/0000-0002-9590-375X

REFERENCES

[1] S. A. M. Tofail, E. P. Koumoulos, A. Bandyopadhyay, S. Bose, L. O'Donoghue, C. Charitidis, *Mater. Today* **2018**, *21*, 22.

[2] R. Goodridge, S. Ziegelmeier, in *Woodhead Publishing Series in Electronic and Optical Materials: Number 88* (Ed: M. Brandt), Elsevier, Cambridge **2017**.

[3] K. Wudy, D. Drummer, M. Drexler, in *The 29th International Conference of the Polymer Processing Society* (Eds: V. Altstädt, Keller Jan-Hendrik, Fathi Amir), AIP Conference Proceedings, Nuremberg, Germany **2014**, pp. 15–19 ISBN: 978-0-7354-1227-91593.

[4] Y. Bao, D. T. Gawne, *Trans. Inst. Met. Finish.* **1991**, *69*, 80.

[5] J. Schäfer, F. Sigeneger, J. Šperka, C. Rodenburg, R. Foest, *Plasma Phys. Control. Fusion* **2018**, *60*, 014038.

[6] A. Wegner, *Thesis Doktor-Ingenieur*, University of Duisburg-Essen (Duisburg), 2015.

[7] J. Wu, X. Xu, Z. Zhao, M. Wang, J. Zhang, *Rapid Prototyp. J.* **2018**, *24*, 813.

[8] G. Flodberg, H. Pettersson, L. Yang, *Addit. Manuf.* **2018**, *24*, 307.

[9] M. Sachs, A. Schmitt, J. Schmidt, W. Peukert, K. E. Wirth, *AIP Conf. Proc.* **2015**, *1664*, 160010.

[10] A. Almansoori, R. Masters, K. Abrams, J. Schäfer, T. Gerling, C. Majewski, C. Rodenburg, *Plasma Processes Polym.* **2018**, *15*, e1800032.

[11] S. Tabibian, F. Arefi-Khonsari, A. Anagri, M. Leturia, A. Moussalem, M. Moscosa Santillan, K. Saleh, Y. Touari, J. Pulpytel, *Plasma Process. Polym.* **2018**, *15*, 1800071.

[12] C. Arpagaus, G. Oberbossel, P. Rudolf von Rohr, *Plasma Process. Polym.* **2018**, *15*, 1800133.

[13] G. M. Vasqueza, C. E. Majewski, B. Hawortha, N. Hopkinson, *Addit. Manuf.* **2014**, *1*, 27.

[14] P. Chen, M. Tang, W. Zhu, L. Yang, S. Wen, C. Yan, Z. Ji, H. Nan, Y. Shi, *Polym. Test.* **2018**, *67*, 370.

[15] K. Wudy, D. Drummer, *Addit. Manuf.* **2019**, *25*, 1.

[16] DuraForm EX Plastic, Month of access, https://www.3dsystems.com/sites/default/files/2017-01/DS_DuraForm_EX_US_0.pdf (accessed: June 2019).

[17] S. Fish, J. C. Booth, S. T. Kubiak, W. W. Wroe, A. D. Bryant, D. R. Moser, J. J. Beaman, *Addit. Manufact.* **2015**, *5*, 60.

[18] C. A. Chatham, T. E. Long, C. B. Williams, *Prog. Polym. Sci.* **2019**, *93*, 68.

[19] C. Schick, R. Androsch, J. W. P. Schmelzer, *J. Phys.: Condens. Matter* **2017**, *29*, 453002.

[20] T. Stichel, T. Frick, T. Laumer, F. Tenner, T. Hausotte, M. Merklein, M. Schmidt, *Opt. Laser Technol.* **2017**, *89*, 31.

[21] M.-S. Sun, C. Nelson, J. J. Beaman, J. J. Barlow, (1990). In J. J. Beaman, *International Solid Freeform Fabrication Symposium*. The University of Texas, Austin, TX, pp. 146–154.

[22] D. Riedlbauer, P. Steinmann, J. Mergheim, *AIP Conf. Proc.* **2015**, *1664*, 160005.

[23] Q. Wan, R. C. Masters, D. Lidzey, K. J. Abrams, M. Dapor, R. A. Plenderleith, S. Rimmer, F. Claeyssens, C. Rodenburg, *Ultramicroscopy* **2016**, *171*, 126.

[24] M. Schmid, A. Amado, K. Wegener, *J. Mater. Res.* **2014**, *29*, 1824.

[25] S. Dadbakhsh, L. Verbelen, O. Verkinderen, D. Strobbe, P. van Puyvelde, J. P. Kruth, *Eur. Polym. J.* **2017**, *92*, 250.

[26] N. S. Murthy, *J. Polym. Sci. Part B: Polym. Phys.* **2006**, *44*, 1763.

[27] L. Feng, Y. Wang, Q. Wei, *Polymers* **2019**, *11*, 727.

[28] S. Rhee, J.-L. White, *J. Polym. Sci., Part B: Polym. Phys.* **2002**, *40*, 1189.

[29] D. J. Skrovanek, S. E. Howe, P. C. Painter, M. M. Coleman, *Macromolecules* **1985**, *18*, 1676.